Journal of Alloys and Compounds 905 (2022) 164217

Contents lists available at ScienceDirect

Journal of Alloys and Compounds

journal homepage: www.elsevier.com/locate/jalcom

Phase control and optimization of photocatalytical properties of samarium doped TiO_2 synthesized by coupled ultraviolet and microwave radiations

Ailton J. Moreira[a,*], Dyovani Coelho[a], Jeferson A. Dias[b], Lucia H. Mascaro[a], Gian P.G. Freschi[c], Valmor R. Mastelaro[d], Ernesto C. Pereira[a]

[a] Department of Chemistry, Federal University of São Carlos, Rod. Washington Luiz, km 235, zip code: 13565-905 São Carlos, SP, Brazil
[b] Institute of Science, Technology and Inovation (ICTIN), Federal University of Lavras campus São Sebastião do Paraíso, 855 Antônio Carlos Pinheiro de Alcântara Avenue, Jardim Mediterranée, zip code: 37950-000 São Sebastião do Paraíso, MG, Brazil
[c] Federal University of Alfenas, Campus Poços de Caldas - MG, Rod. José Aurelio Vilela, BR 267, Km 533, 11999, University City, zip doce: 37715-400 Poços de Caldas, MG, Brazil
[d] São Carlos Institute of Physics, University of São Paulo, zip code: 13566-590120 São Carlos, SP, Brazil

ARTICLE INFO

Article history:
Received 1 December 2021
Received in revised form 22 January 2022
Accepted 11 February 2022
Available online 13 February 2022

Keywords:
Environmental Pollution
S-triazines
Photocatalysis
Mechanisms
TiO_2 polymorphs

ABSTRACT

The scientific community has been looking for strategies to synthesize active catalysts under Ultraviolet_Visible (UV_Vis) light to atrazine (ATZ) degradation. In this study, we applied for the first time the microwave (MW) energy and a Microwave Discharge Electrodeless Lamp (MDEL) as an UV_Vis light source to synthesize photocatalysts. The synergistic use of MW_UV_Vis energies allowed obtaining Sm-doped TiO_2 with photoactivity under UV-A light (365 nm) to degrade ATZ. Different characterization analyzes showed that Sm^{3+} was inserted into the TiO_2 lattice and prevented the conversion of anatase into rutile, in addition to giving rise to brookite phase, which increase under MDEL assisted synthesis. Different techniques proved the doping, and especially photoluminescence (PL) showed that electrons are excited to f levels of Sm^{3+} and can be trapped in the structural defects of the photocatalyst to be consumed later. Moreover, the catalyst synthesized under MDEL irradiation (STiM) showed lower recombination rates and a performance to degrade ATZ of 45% and 15% higher than pristine TiO_2 (Ti) and Sm-doped TiO_2 (STi), respectively. Photocatalytic degradation mechanism was unveiled by monitoring Desethyl-atrazine (DEAT), Desisopropyl-atrazine (DIAT), and Hydroxy-atrazine (HAT), which are by-products of ATZ. The doped materials showed high efficiency to activate the ATZ hydrolysis reaction, while the water oxidation to generate $^{\bullet}OH$ and converted ATZ to HAT was more pronounced in STiM. We proved through radical probe tests that STiM produces more hydroxyl radicals and that its photoactivity remains even after 4 application cycles.

1. Introduction

According to the United Nations (UN), the global population will reach the mark of 9 billion inhabitants by the year 2050 [1]. Thus, the demand for food, which is already high, tends to increase, requiring different strategies from the agricultural industry to meet the new global needs for food production [2]. It so happens that one of the current strategies and that should be continued for years to come to increase food production is the use of pesticides. According to literature data, annually 2 million tons of pesticides are consumed worldwide, and the herbicide class represents 47.5% of this total [3]. As a consequence of the massive use of pesticides, numerous cases of environmental pollution around the world have been reported, and the main impacted ecosystems are soil and water [3,4]. Atrazine is a widely used herbicide in agriculture worldwide, but reports of environmental persistence, toxicity to living beings, and carcinogenicity have made its use be reevaluated in many countries in recent years, while its application this banned in the European Union since 2007 [5]. Even so, continental-dimensions countries like China, USA, Brazil, Argentina, and India consume high amounts of atrazine and the environmental impacts are evident due to the persistence of this herbicide to degradation by natural processes [5,6]. To make the use of atrazine even more problematic, recent studies have shown that degradation products are also harmful to the environment, with

* Corresponding author.
E-mail address: aijomoquim@gmail.com (A.J. Moreira).

https://doi.org/10.1016/j.jallcom.2022.164217
0925-8388/

chlorinated by-products being more toxic than hydroxylated by-products [7,8].

As technologies based on advanced oxidation processes (AOP) can produce hydroxyl radicals, the degradation of ATZ to form hydroxylated and less toxic products is preferred [9–11]. Thus, the use of semiconductor materials with photoactivity under UV_Vis light irradiation has been investigated to form reactive oxygen species from the oxidation of water [12,13]. TiO_2 is a semiconductor widely applied in heterogeneous photocatalysis due to its photoactivity under UV light, however, new synthetic strategies have been investigated to improve its performance under light irradiation with a wavelength close to the visible region ($\lambda \geq 320$ nm) [14,15]. Rutile, anatase, and brookite are the main TiO_2 polymorphs obtained by applying different synthetic routes, and only anatase and brookite show photoactivity for application in heterogeneous photocatalysis [16,17]. Rutile inactivity is due to the trapping of photoexcited electrons in deep structural defects, while in anatase electrons are directly excited from VB to CB to preferentially promote reduction reactions [18]. Interestingly, brookite is a polymorph of difficult obtaining, but it has intermediate properties between rutile and anatase. In brookite, the photoexcited electrons are trapped in moderate depth structural defects, allowing the migration to CB in conditions of high electron concentration to occur by the multielectron process [18,19]. Consequently, the continuous feeding of the redox pairs (h^+ - e^-) increases the catalytic activity of brookite to promote both oxidation reactions in VB and reduction in CB.

Anatase and brookite are TiO_2 metastable polymorphs that initially form under high-energy synthetic conditions and tend to be converted into rutile, which is the most stable phase [20]. However, some synthetic strategies such as insertion of dopants with greater ionic radius than Ti^{4+} can restrict unit cell volume compression and thus prevent conversion to rutile. Furthermore, anatase and brookite are preferably obtained by hydrothermal routes, and studies show that brookite can be stabilized by reduction [21]. According to the literature, the synthetic route to obtain brookite is complex and depends on numerous factors [21]. However, for Ti^{4+} precursor solutions, the hydroxylation favors the formation of anatase-brookite or brookite-anatase in detriment to the rutile formation [22,23]. As Ti^{4+} ions have free "d" orbitals, they accept electrons from OH^-, H_2O, and other nucleophiles to form Ti^{n+} complexes that are more efficient in controlling precipitation kinetics and thus, form preferentially the anatase-brookite photoactive polymorphs [22]. In the presence of Cl^-, F^- or OH^- ions, brookite formation occurs due to anions adsorption on the surface of the crystals, which increases the negative charge density in the grain and guides the interfacial interaction to form brookite [21,22].

Thus, to ATZ photocatalysis by reduction processes in CB, the anatase is preferred while brookite shows greater potential to trigger water oxidation processes in VB and form the hydroxyl radicals that will be responsible for oxidizing ATZ in HAT. However, achieving photoactivity under light irradiation close to the visible region is advantageous in photocatalytic processes, and the choice for dopants with electronic levels fed by electrons with this energy is a preferable choice [24]. Therefore, Sm^{3+} is a potential dopant to obtain photoactive TiO_2 under UV-A_Vis light irradiation. Its electronic structure allows the trapping of photoexcited electrons in the f sublevel, which, added to the trapped electrons in brookite defects, can optimize the redox pairs formation continuously due to the multielectron process [18,25]. Furthermore, Sm^{3+} has an ionic radius (0.96 Å) greater than Ti^{4+} (0.75 Å) and can prevent the conversion of anatase/brookite to rutile due to the volume restriction of the unit cell [26]. Studies show that TiO_2 doped with Sm has photocatalytic activity on visible, and the anatase phase is preferentially formed in the presence of this dopant even under heat treatment conditions of up to 700 °C [26,27].

The mixture of anatase and brookite also shows advantages for applications in photocatalysis due to the sharing of electrons between these polymorphs, because while the holes in the VB are preferentially formed in the brookite, the excess of electrons is verified in the CB of the anatase [28,29]. Thus, reaching a synthetic route without the insertion of toxic reagents and allowing to obtain a reductive environment to produce brookite is a challenge that can be overcome with the use of light. As MDELs are composed of different elements that, when activated by microwave radiation, emit light spectra with highly energetic wavelengths, these light sources when added to the reaction vessel can promote redox reactions to increase the concentration of electrons in the synthetic medium [30,31]. Briefly, MDEL emits high-energy radiation with the potential to promote the water photolysis and produce hydroxyl radicals ($^{\bullet}OH$), protons (H^+), and hydrated electron ($e^-_{(aq)}$) [31,32]. Highly reactive, the $^{\bullet}OH$ and $e^-_{(aq)}$ act as nucleophiles to react with the "d" orbitals of Ti^{4+}, in addition to promoting other secondary reactions depending on the precursors used. Thus, in the presence of MDEL, the growth of TiO_2 grains can have their surface rich in $^{\bullet}OH$, while $e^-_{(aq)}$ can be consumed to occupy the initially free "d" orbitals [22]. As these conditions are favorable to obtain anatase-brookite, the use of MDEL shows potential for application in synthetic steps. Another advantage to be highlighted is that the hydrothermal condition can be maintained, and the synergistic effect of microwave and UV_Vis radiation from MDEL can effectively contribute to creating highly favorable environmental conditions for producing brookite. Therefore, this study shows for the first time the application of the hydrothermal method assisted by MW_UV_Vis radiation to produce Sm-doped TiO_2. While the hydrothermal condition forms in preferential order the anatase and brookite phase, the insertion of MDEL in the reaction vessel aims to create a reductive environment to produce the brookite phase. The choice of Sm^{3+} as a dopant aims to restrict the contraction of the lattice to preferentially form anatase and brookite. In addition, the electronic levels *f* of this rare earth metal contribute to the trapping of photoexcited electrons in moderate depth defects of the brookite phase. These trapped electrons can contribute to the multielectron process and optimize the continuous formation of redox pairs to promote ATZ photocatalytic reactions in VB and CB.

2. Experimental

2.1. Nanomaterials synthesis

To obtain pristine TiO_2 4.2 mL of titanium tetraisopropoxide (98%, Sigma Aldrich) was dispersed in 20 mL of a 20% (v v^{-1}) aqueous isopropanol solution (99%, Sigma Aldrich). The Sm-doped TiO_2 was obtained adding 50 mg of $SmCl_3{\cdot}6H_2O$ (99%, Sigma Aldrich) at Ti^{4+} precursor solution to achieve a Sm/Ti theoretical molar ratio (1 mol %). The mixture was kept under magnetic stirring for 1 h for homogenization and transferred to a 75 mL Teflon vessel (MARSXpress). Into one of the vessels, a cadmium electrodeless discharge lamp (MDEL) of the Anton Paar brand (catalog no. = 16847) was added to the assisted synthesis by MW_UV_Vis radiation. The other vessel was used for the synthesis assisted only by MW radiation, without the MDEL. To clarity, the synthesis methods have been illustrated in Fig. 1.

The reaction vessel was then taken to the microwave equipment (Mars 6 CEM®) and a heating ramp from 25 to 160 °C was applied in 10 min. Then, the microwave power was set at 300 W and maintained for another 30 min. At the end of the microwave-assisted synthetic step, the system was naturally cooled to room temperature. The mixture was then centrifuged and the solid was washed with 10 mL of ethanol (3 times). Two heat treatment steps were conducted for all materials. In the first step, the samples were kept in a borosilicate glass beaker, heated to 200 °C at a heating rate of

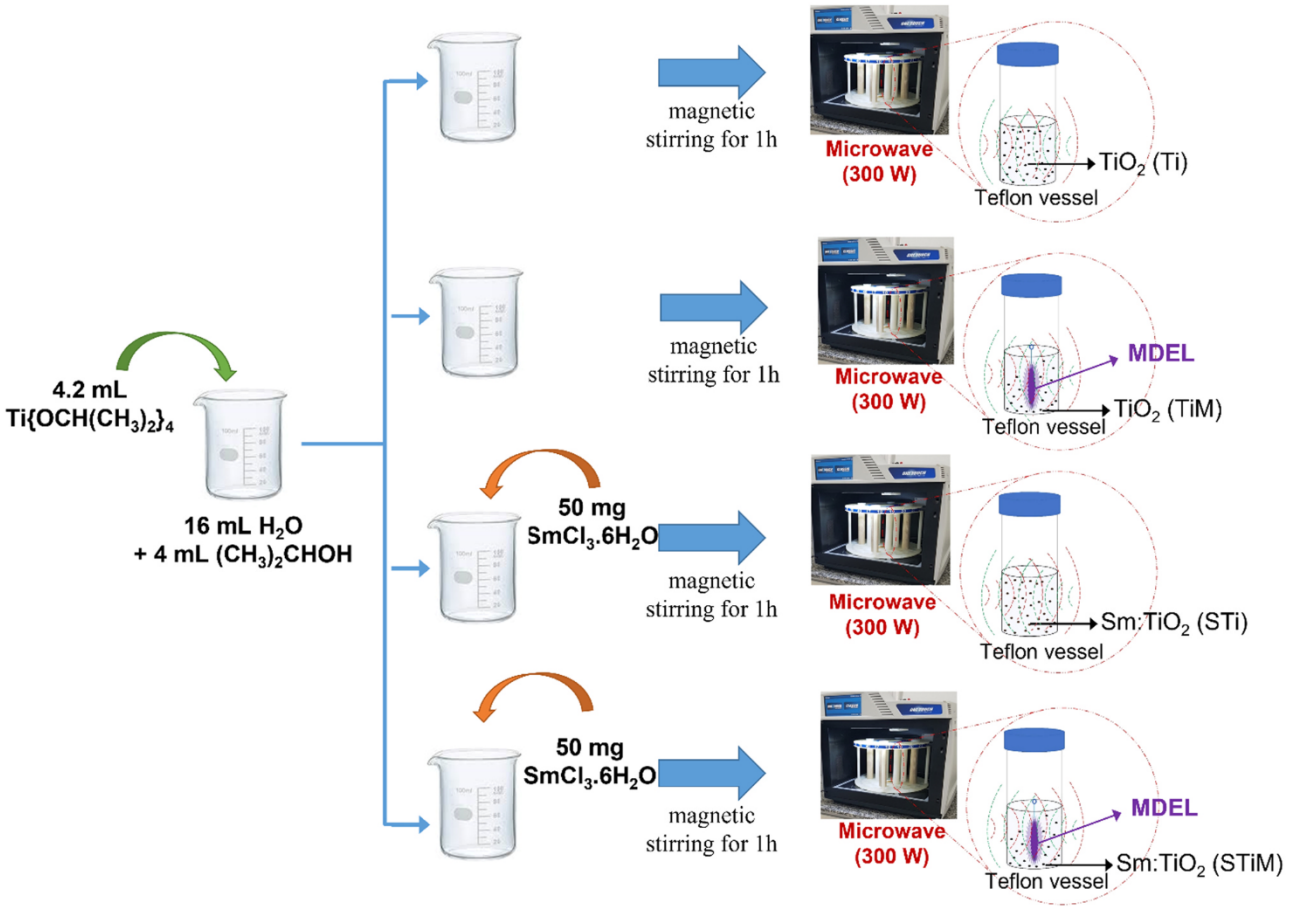

Fig. 1. Representative methods to the nanomaterials synthesis by the MW_UV_Vis radiation assisted hydrothermal method.

5 °C min^{-1}, and kept at the final temperature for 2 h. At the end of this step, the samples were naturally cooled to room temperature, macerated for deagglomeration. The fine powder was transferred to an alumina capsule, being a small portion separated for XRD analysis. In the second stage of heat treatment, the samples were calcined at 600 °C under a heating rate of 5 °C min^{-1} and kept at this temperature for 2 h. After cooling, the samples were identified and submitted to characterization analysis and photocatalytic application.

2.2. Materials characterization

The crystallinity of samples was analyzed by X-ray diffractometry (XRD) using a D/Max-2500PC diffractometer (Rigaku, Japan) with Cu Kα radiation (λ = 0.154184 nm), angle of diffraction 2θ ranging from 10° to 110°, and a scanning step of 0.02° min^{-1}. The phases were indexed to crystal structures based on crystallographic cards from the Inorganic Crystal Structure Database (ICSD), anatase (ICSD card no. 242104 [33]), rutile (ICSD card no. 256875) [34], and brookite (ICSD card no. 257865) [35]. The lattice parameters were obtained by Rietveld refinements using the GSAS-EXPGUI software [36]. The Le Bail method was used to acquire the instrument parameters based on Yttrium oxide (99.99%, Sigma -Aldrich) as an instrument standard. Also, the Mercury 4.0 software [37] was used to represent the structures according to the crystallographic information from the crystallographic cards aforementioned. Finally, the crystallite sizes were calculated applying the Scherrer equation [38].

Micro-Raman spectroscopy was applied to evaluate the materials' crystalline structures in the short- and medium-range order. The assays were realized by a HORIBA Jobin Yvon LabRam spectrophotometer (model HR800) in the region of 70–1000 cm^{-1}. A laser light of 632.8 nm was used as the excitation source. The laser was focused on the surfaces of the powder through a 50x objective lens. An exposure time of 60 s and 15 repetitions were used to collect the spectra. Photoluminescence (PL) spectra were recorded in Fluorolog Horiba Jobin Yvon equipment (model FL3–22). A continuous-Xe lamp (450 W) coupled to a monochromator was used to excite the samples at 280 nm and 360 nm. For PL analysis, 10 mg of each one powder was dispersed in 10 mL of Milli-Q water by sonicating the suspensions for 10 min in an ultrasound bath. Equal aliquots of the suspensions were rapidly transferred to quartz crucibles and analyzed in the spectrophotometer. Once the experimental setups were the same for all the samples, the spectra were normalized concerning the water band (Raman signal) used as the dispersion medium.

The morphology was characterized by Field Emission Scanning Gun Electron Microscopy (FEG-SEM) operated at 5 kV (Supra 35-VP, Carl Zeiss). The high-resolution transmission electron microscope (HR-TEM) images of the nanoparticles were obtained by a Jem-2100 LaB6 (Jeol, Tokyo, Japan) under an accelerating voltage of 200 kV coupled with an INCA Energy TEM 200 (Oxford, Abingdon, UK). Diffuse reflectance UV–vis spectra were obtained using a UV-Vis spectrophotometer with integrating sphere (ISR-2600 Plus, Shimadzu) at the range of 200–800 nm. Here, the bandgap energy (Eg) was calculated by constructing Tauc plots based on the conversion of diffuse reflectance into the rate of absorption coefficient and scattering, according to the Kubelka-Munk model [39].

The chemical analysis of samples surface was performed by X-ray photoelectron spectroscopy (XPS) using a conventional XPS spectrometer (Scienta Omicron ESCA +) with a 128-channel hemispheric

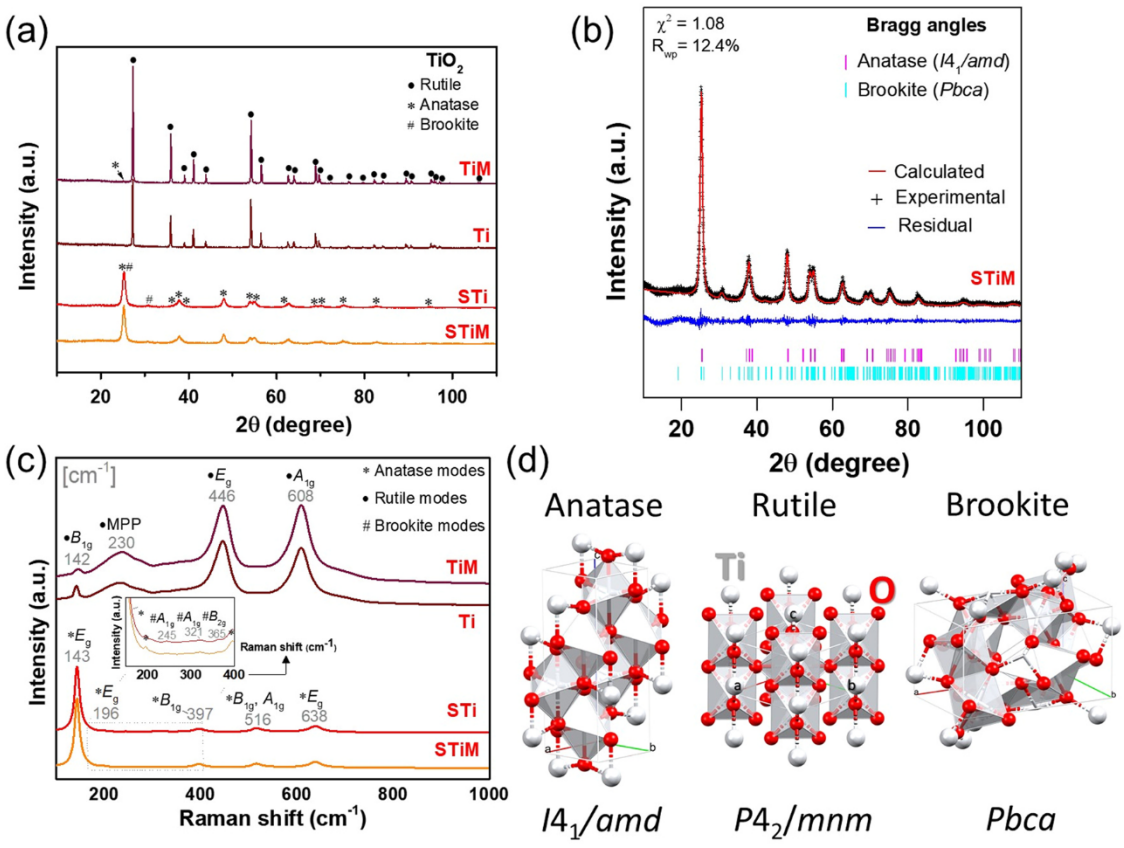

Fig. 2. XRD pattern (a), Rietveld refinement of the STiM (b) sample after heat treatment at 600 °C. Raman spectrum of the materials (c) and structure of the TiO_2 polymorphs (d).

analyzer (EAC2000) with monochrome Al Kα radiation (h ν = 1486.6 eV) as the excitation source. The high-resolution XPS spectra were recorded at constant pass energy of 20 eV with 0.05 eV per step. During the measurements, a charge neutralizer was used to avoid electrically charging the samples. The XPS spectra were calibrated by using the C1s aliphatic component from C 1 s peak, which binding energy is located around 284.8 eV. The XPS data were analyzed using the Casa-XPS software. Composition analysis is done by inductively coupled plasma optical emission spectroscopy (ICP - OES, Thermo, iCAP 6000).

2.3. Photocatalytic assays

To investigate the photocatalytic properties of materials, the first assay was performed with the model molecule Rhodamine B (RhB). Thus, 10 mL of a 5 mg L^{-1} Rhodamine B (RhB) solution was transferred to a glass beaker added with 5 mg of the materials, individually, and kept in the dark for 30 min under stirring to achieve the adsorption equilibrium. Then, the mixture was exposed to UV-A (365 nm, 75.7 mW cm^{-2}) radiation using an LED lamp (M365PL1 model, THORLABS). The irradiance was mediated by a spectroradiometer (SPR-4002 model, Luzchem). During the degradation period (0–60 min), all samples were maintained under constant stirring and the system temperature was controlled at 25 °C. After each degradation time, the samples were centrifuged and analyzed by spectrophotometry in the range of 200 at 800 nm. To determine the C/Co ratio, the centered absorbance peak in 553 nm was selected. One second photocatalytic assay was carried out applying the ATZ emerging contaminant to investigate in depth the photocatalytic mechanisms of the different materials. Therefore, the photocatalytic activity of nanomaterials was tested from an 8.5 mg L^{-1} atrazine aqueous solution which was prepared after appropriate dilution of a 1000 mg L^{-1} stock solution prepared from salt pure (ATZ - Sigma-Aldrich, ˃ 99%). Therefore, 10 mL of ATZ solution was transferred to a glass beaker added with 5 mg of the materials, individually, and kept in the dark for 30 min under stirring to achieve the adsorption equilibrium. Then, the mixture was exposed to UV-A radiation using the same LED lamp described above. During the degradation period (0–300 min), all samples were maintained under constant stirring and the system temperature was controlled at 25 °C. After each degradation time, the samples were filtered in a 45 µm membrane and analyzed by HPLC – UV.

Probe assays for hydroxyl radicals (˙OH) were performed by the reaction with coumarin following the photoluminescent method described in Moreira et al. [40]. In these assays, the irradiation time was fixed in 120 min. Reuse assays were carried out in up to 4 cycles for the material that showed better performance in ATZ degradation. Here, no pretreatment was applied to the materials before reapplication.

3. Results and discussion

3.1. Nanomaterials characterization

Fig. 2 shows the XRD patterns of the TiM, Ti, STi, and STiM samples with intense and well-defined diffraction peaks due to the high crystallinity of the materials. The TiM and Ti samples (Fig. 2a) is composed mostly of the rutile polymorph (space group $P4_2/mnm$) [34], while the STi and STiM samples were composed of a mixture of anatase and brookite polymorphs (space groups $I4_1/amd$ [33] and *Pbca* [35], respectively). Rutile polymorph found in the TiM and Ti samples corroborates the literature data, which indicate the preferential formation of this crystalline phase when TiO_2 is treated at temperatures ≥ 600 °C [41–43]. However, the STi and STiM samples

Table 1
Parameters obtained by Rietveld refinement of the XRD patterns of the TiM, Ti, STi and STiM samples treated at 600 °C.

		STiM	STi	Ti	TiM	ICSD #242104[30]	ICSD #257865[43]
Rutile wt (%)		–	–	100	99.5	–	100
Anatase wt (%)		88	92	–	0.05	100	–
Brookite wt (%)		12	8	–	–	–	–
a, *b* (Å)		3.7876(2)	3.7885(2)	4.5943(1)	4.5940(1)	3.7847(1)	4.6189(4)
c (Å)		9.501(1)	9.498(1)	2.961(1)	2.9602(1)	9.5140(3)	2.9357(4)
V (Å^3)		136.3	136.3	62.5	62.5	136.3	62.6
R_{wp}		12.3	12.4	13.3	15.8	–	–
X^2		1.09[b]	1.08	1.20[c]	1.84[c]	–	–
Crystallite size (nm)[a]	200 °C	5	3	3	–	–	–
	600 °C	10	9	54	52	–	–

[a] Calculated from Scherrer equation of the phase with greater weight percentage.
[b] Lattice parameters from the phase with greater percentage – Anatase phase.
[c] Lattice parameters from the phase with greater percentage – Rutile phase.

did not show the presence of the rutile polymorph even being obtained under the same temperature conditions, it indicates that the dopant (Sm) inhibited the conversion of anatase into rutile. This inhibitory effect that Sm exerts on the conversion of anatase to rutile has already been reported in previous studies [26,27], suggesting that the larger crystal radius of Sm^{3+} (1.10 Å, in octahedral coordination) compared to the crystal radius of Ti^{4+} (0.75 Å, in the same coordination) limit the crystalline lattice contraction and, consequently, the phase conversion at 600 °C [26,27]. To support this hypothesis, Fig. S1 shows the XRD patterns of the samples obtained with the first heat treatment at 200 °C. The low-intensity diffraction peaks at positions 2θ (degree) = 37.2°, 47.2°, and 53.4°, and the highest intensity peak at 25.2° was found for the materials, being compatible with the anatase phase (ICSD 242104) [33]. Therefore, these results confirm that under conditions of low temperature (200 °C) the anatase polymorph is preferentially formed. The crystallite size was calculated by the Scherrer equation for the samples treated at 200 and 600 °C. Crystallites with sizes of 3 nm for Ti and STi, and 5 nm for STiM confirm that the microwave-assisted synthetic method followed by thermal treatment at 200 °C was sufficient to initiate the crystallization process.

Even at identical conditions of temperature, dopant nature (Sm), and theoretical amount of this dopant (1 mol%), the crystallite size calculated for STiM (5 nm) was ~ 45% larger than the crystallite size calculated for STi (3 nm) when treated at 200 °C. Here, the unique difference between the synthetic methods was the MDEL insertion to obtain STiM, suggesting that the UV_Vis radiation source was responsible for increasing the STiM crystallization kinetics. This hypothesis is supported by the insignificant difference in crystallite size observed for the Ti and STi samples that were not irradiated by the MDEL. To explore the effect of radiation on the crystallization process of the STiM sample, Fig. S2 shows the MDEL emission spectrum that was measured when this light source was activated by microwave equipment operating at 300 W. High-intensity peaks for the visible and near-infrared region (700–900 nm), as well as low-intensity peaks for the UV-C (193 nm) to UV-A (400 nm) and visible (400–700 nm), were identified. Even with low intensity, wavelengths in the 193–247 nm range, especially, transport energies capable of promoting the water photolysis for generating reactive species such as $^{\bullet}OH$, $O_2^{\bullet-}$, $e^-_{(aq)}$, H^+ [31,44]. Furthermore, these wavelengths show the potential to change the chemical composition of the reaction medium during the crystallization step, in addition to promoting the electronic transition in the nanoparticles that are continuously growing [45]. Thus, for a detailed analysis of the crystal structure of the materials, Rietveld refinement was applied, and good convergence was obtained. This is supported by the graphical analysis of Fig. 2b showing the experimental and calculated curves overlapped and by the quality parameters R_{wp} and χ^2 shown in Fig. 2b, Fig. S3 and Table 1. Parameters were shown in Table 1 for all samples treated at 600 °C.

The percentage distribution of each TiO_2 polymorph in the synthesized samples was 0.5% anatase and 95% rutile for TiM, 100% rutile for Ti, 92% anatase and 8% brookite for STi, and 88% anatase and 12% brookite for STiM. The same qualitative polymorphic composition for the different nanomaterials was also confirmed by Raman spectroscopy analysis. Fig. 2c shows three Raman-active phonon modes from the rutile phase (Γ: $A_{1g} + B_{1g} + E_g$), in addition to the multi-phonon mode (MPP) for the TiM and Ti samples. To the STi and STiM samples were identified the six Raman-active phonon modes of the anatase polymorph (Γ: $A_{1g} + 2B_{1g} + 3E_g$), and three other low-intensity Raman-active phonon modes for the brookite polymorph (Γ: $2A_{1g} + B_{2g}$) [20,40,41]. In addition to the dopant inhibiting the conversion of anatase to rutile, the data also confirm its contribution to forming the brookite polymorph in low quantity, corroborating the XRD results. This effect of the dopant on the anatase-brookite phase transition is due to the unit cell volumes of the respective polymorphs that were structurally represented in Fig. 2d. The literature shows that the unit cell volume of brookite (257 Å^3) [35] can be up to 47% larger than anatase and 76% larger than rutile [46]. Already unit cell volumes calculated in this study were 62.5 Å^3 for the rutile phase in TiM or Ti and 136.3 Å^3 for the anatase phase in STi and STiM, while the low mass percentage of brookite did not allow us to find experimentally the volume for this polymorph with confidence. Either way, an expansion in unit cell volume would be needed to convert rutile/anatase to brookite, or shrinkage in volume would be needed to convert brookite to anatase/rutile, but this detailed mechanism is still controversial [21,46]. However, our finding that the samples were initially composed of anatase at 200 °C suggests that the phase conversion at 600 °C occurred by unit cell volume retraction to form rutile, while the formation of up to 12% of brookite for STiM may be related to the grain growth in the contour region where Sm^{3+} is present. Thus, by presenting a crystal radius 22% greater than Ti^{4+}, Sm^{3+} prevents lattice contraction and consequently conversion into anatase. This hypothesis is corroborated by the crystallite sizes calculated for the samples after thermal treatment at 600 °C, which showed slightly higher values for STiM when compared to STi, possibly due to the contribution of the greater amount of brookite. Also according to the literature, the thermodynamic stability of polymorphs is achieved for crystallites with a size close to 11 nm for anatase, 11–35 nm for brookite, and > 35 nm for rutile [28,45,47], agreeing with the calculated values (Table 1).

Farther to the influence of the dopant in the brookite formation, the refinement data also show that the brookite percentual amount was increased by 50% in the synthetic system containing MDEL (STiM) when compared to the system without MDEL (STi). To understand the influence of MDEL on phase conversion, the literature reports that the brookite phase is preferably obtained in a reaction medium with reductive potential and is capable of providing surface electrons to preferentially crystallize this polymorph [21,45]. Thus,

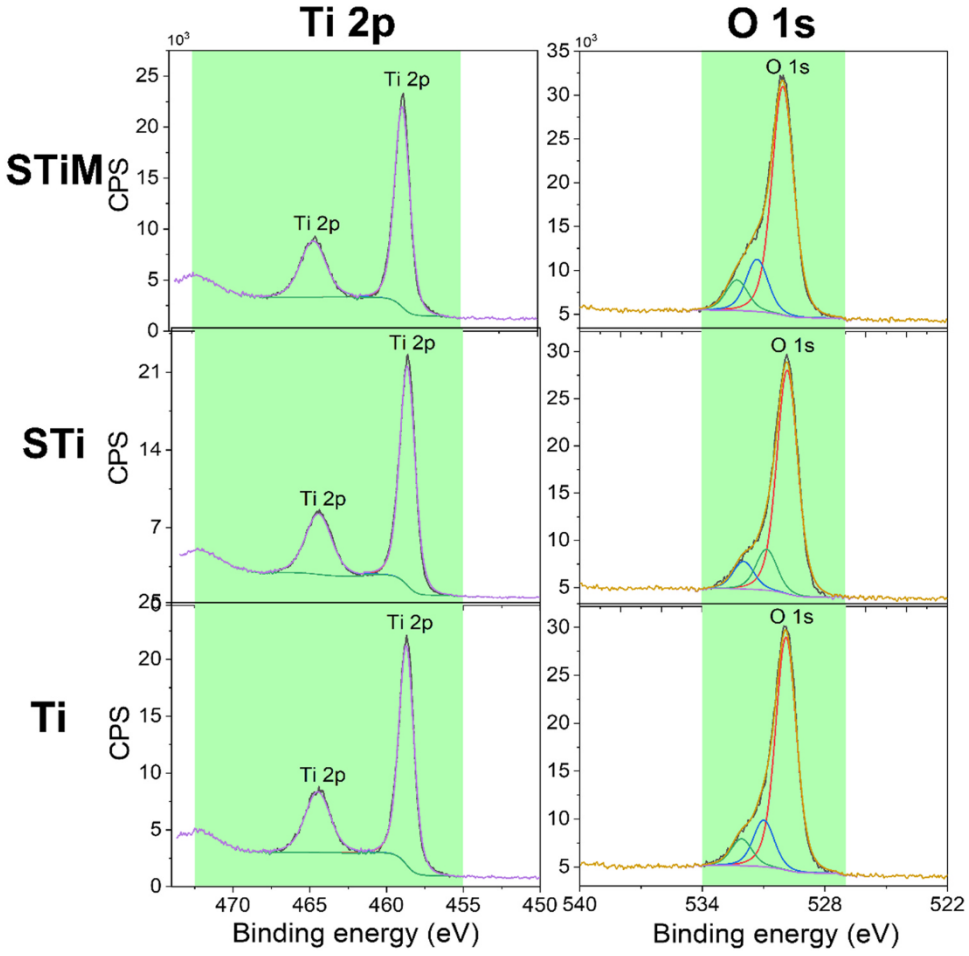

Fig. 3. XPS spectrum of Ti2p and O1s of the Ti, STi, and STiM samples.

the high energy wavelengths emitted by MDEL (Fig. S2) can excite the electron (e^-) from VB to CB in the crystals in formation, giving rise to a more reductive surface in STiM to form more brookite in Sm^{3+} presence. Additionally, the photolysis of water promoted by MDEL also originates reactive oxygen species, which act in the oxidation of the organic precursor (titanium isopropoxide) to increase the concentration of electrons in the reaction medium, favoring the crystallization of brookite.

As the TiM and Ti samples show significant similarities in terms of crystalline phase composition, some characterization assays were performed only for Ti. Thus, Ti, STi, and STiM samples surfaces were investigated by the high-resolution X-ray photoelectron spectroscopy (XPS) technique and the characteristics peaks of Ti 2p, O 1s, C 1s, were found for all materials. As shown in Fig. 3, the peaks centereds at 458.1 and 464.0 eV were attributed to the Ti $2p_{3/2}$ and Ti $2p_{1/2}$ levels of the Ti^{4+} ion, respectively, with an energy separation around 6 eV, characteristic of the TiO_2 compound [3]. Furthermore, the satellite peak centered at 471.0 eV was found in all samples and is also characteristic of the TiO_2 compound [48]. The high-resolution XPS spectrum of O 1s peak centered at 530.0 eV was decomposed into three different peaks: the peak centered around 530.1 eV is related to the O-Ti bond of the TiO_2 crystalline lattice and also O-Sm like in the Sm_2O_3 compound [49,50]. The two additional peaks centered on 531.3 eV and 532.3 eV were respectively attributed to the hydroxyl group (OH) and the C–O bonds. We did not observe significant differences in O 1s XPS spectra between the three samples.

Samarium identification by XPS spectroscopy is often related to the presence of peaks centered at 1071 and 1105 eV, which are attributed to the Sm $3d^{5/2}$ and Sm $3d^{3/2}$ levels, respectively [26,27,51]. However, as can be observed in Fig. S4, at this same energy region, we also observed the presence of Ti LMM XPS peaks on the TiO_2 sample without samarium (Ti sample) [52]. This means that there is a superposition between the Sm 3d and Ti KLMM XPS peaks in the samples which contain titanium and samarium. Therefore, by using the Sm 3d level XPS peaks, it is not possible to determine the amount and evaluate the electronic properties of samarium when titanium is present in the same sample. Thus, to confirm the presence and the amount of Sm íons in the STi and STiM, measurements elemental analysis by ICP OES were performed and an Sm content equal to 0.08 mol% for STi and 0.05 mol% for STiM were determined.

The SEM images show a high agglomeration of the Ti sample with multifaceted structures without defined morphology, which is characteristic of the rutile polymorph [53], while STi and STiM show spherical geometric (Fig. S5). Unfortunately, it is not possible to define the grain contour from the SEM images and estimate the nanoparticles size distribution for STi and STiM samples. However, as can be seen in Fig. S5, the TEM analyses show a spherical shape for these samples. The histograms in Fig. S6 show a 12.4 ± 4.6 nm and 12.3 ± 3.9 nm particle size to the STiM and STi, respectively. Further, it is observed a positive skewness of 1.7 and 1.0 to STiM and STi sample, respectively. The values of the skewness indicate a left-leaning curve, which describes an asymmetric distribution of the nanoparticle size. Fig. 4a,b showed the HR-TEM images of STi and STiM samples, which exhibit the lattice fringes and the d-spacing for some of them calculated by FFT analysis and its inverse in some lattice fringe domains. Table S1 are shown the lattice fringe distances, (hkl) index, diffraction angle expected, and the assigned

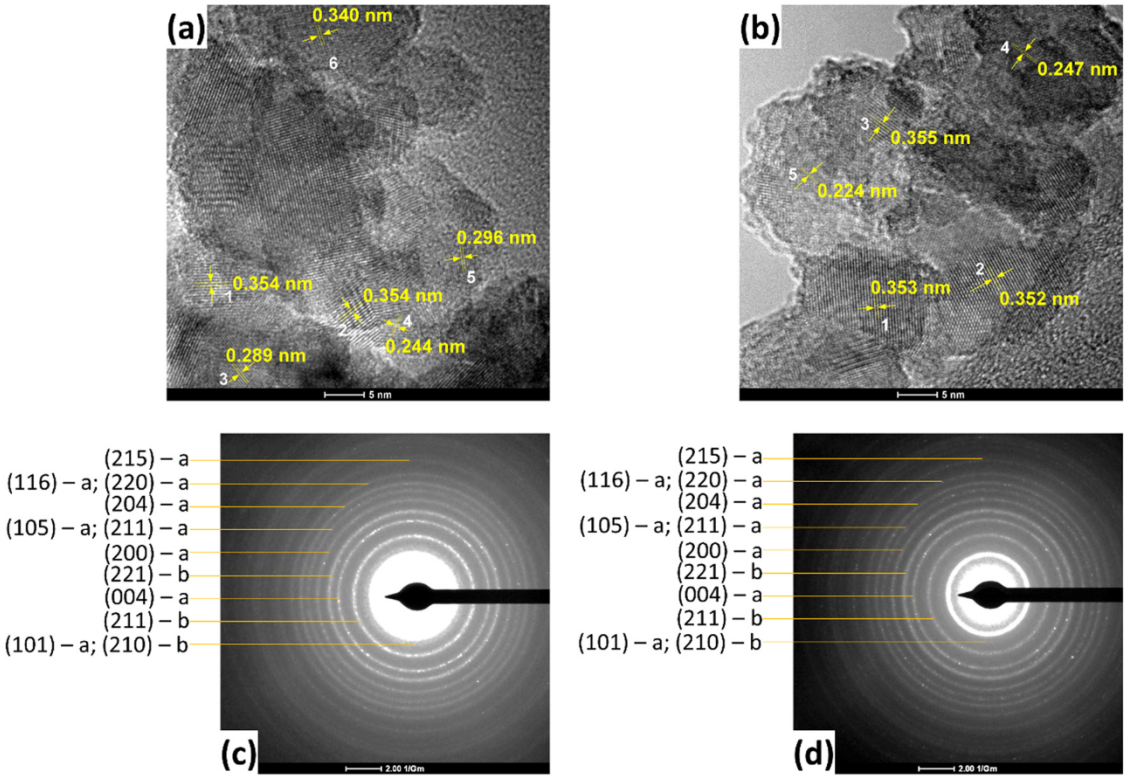

Fig. 4. TEM images of Sti (a) and STiM (b) with the lattice parameter for some crystalline planes. SAED patterns of STi (c) and STiM (d) samples with the main diffraction rings identified by the correspondent (hkl) index. The letter "a" indicates anatase phase and "b" brookite phase.

crystalline phase for each measurement in Fig. 4a and b. In respect to STi and STiM samples were observed lattice fringes typical for anatase (0.352, 0.353, 0.354 and 0.244 nm) and brookite (0.289, 0.296, 0.340, 0.247, and 0224 nm). Also, the SAED patterns (Fig. 4c,d) are in agreement with the lattice fringes distances measured and corroborate with the XRD of the samples after the addition of Sm.

Fig. 5a showed the diffuse reflectance spectra of the samples when irradiated in the range of 300–500 nm. The TiM and Ti samples showed a transition at 400 nm, while the transition verified for STi and STiM was close to 350 nm with a slight shift to a longer wavelength region in the case of the STiM sample. Bandgap energy (E_{gap}) was calculated from the diffuse reflectance data. Here, it was considered for calculation that rutile has gap energy for direct transition (n = 2) and the anatase phase has gap energy for indirect transition (n = 0.5) [53]. The calculated values were E_{gap} = 3.02 eV for TiM, E_{gap} = 3.05 eV for Ti, E_{gap} = 3.26 eV for STiM and E_{gap} = 3.29 for STi (Fig. 5b). For STi and STiM, the bandgap energy slightly decreased for STiM, synthesized in the presence of MDEL, finding a range between energy levels slightly lower compared to the STi sample.

PL spectra obtained after excitation with λexc.= 360 nm (Fig. 5c) shows that no emission is verified for the Ti sample which represents pure TiO_2. To STi and STiM samples, 3 emission peaks centered at 585, 613, and 666 nm were identified and represent the electronic transitions from the 4f level to $^4G_{5/2}$ (585 nm), $^6H_{7/2}$ (613 nm), and $^6H_{9/2}$ (666 nm). As they are characteristic emissions of Sm^{3+}, the presence of the dopant in the structure of TiO_2 can be confirmed, as well as its contribution to the electronic transition processes [54]. Broadband spectra with shoulders in some regions of the graphic contour were identified for STi and STiM (Fig. 5c) and seeking to extract more detailed information from the electronic transition processes, Fig. 5c was deconvoluted in Fig. 5d (STiM) and Fig. 5e (STi). The deconvolution showed that there is no significant difference for the PL spectrum of the STi and STiM samples, which exhibited with good fit the peaks centered at 580, 585, 613, 624, and 666 nm. The normalized emission intensity that was shown in Fig. 5d confirms that the recombination rates in STi are higher than the recombination rates in STiM. Since TiO_2 acts as a host for Sm^{3+}, it is possible to state that in the electronic excitation process, the energy absorbed by TiO_2 promotes the separation of charge carriers to generate the e^-/h^+ pair. However, before recombination can occur, the host excited electron is transferred to the Sm^{3+}, keeping it trapped in its band structure complex for longer in STiM than in STi [55]. In addition, the Rietveld refinement confirmed the greater amount of mixing of the anatase-brookite phases, which also act to delay the recombination process [29]. Thus, the characterization analyzes suggest that STiM photoactivity should be greater than STi under 360 nm irradiation. Furthermore, the decrease in recombination rates may favor the production of reactive oxygen species in VB - CB to oxidize organic molecules aiming the treatment of contaminated water. Therefore, photocatalytic degradation assays were performed under 365 nm LED light (UV-A).

3.2. Photocatalytic assays

3.2.1. Photocatalytic degradation of RhB

Fig. 6a shows the RhB degradation curve expressed as a C/Co ratio after photolytic and photocatalytic processes at different times of exposure to UV-A light irradiation. In the dark adsorption equilibrium assay, the RhB removal was 6% for Ti, 7% for STi, 9% for TiM, and achieve the maximum value of 15% for STiM within 30 min, showing that the removal by adsorption was not significant. When the UV-A light source was activated, the RhB degradation by the photolytic mechanism was only 10% in 5 min and achieve a maximum value of 23% in 60 min. However, with the photocatalytic process in the presence of the Ti sample, the removal was only 15% for a time of up to 15 min, being comparable to the low efficiency of photolysis, while TiM achieve 45% removal in 15 min. Notably, the RhB removal was 81% for STi and 97% for STiM within 15 min, highlighting the high

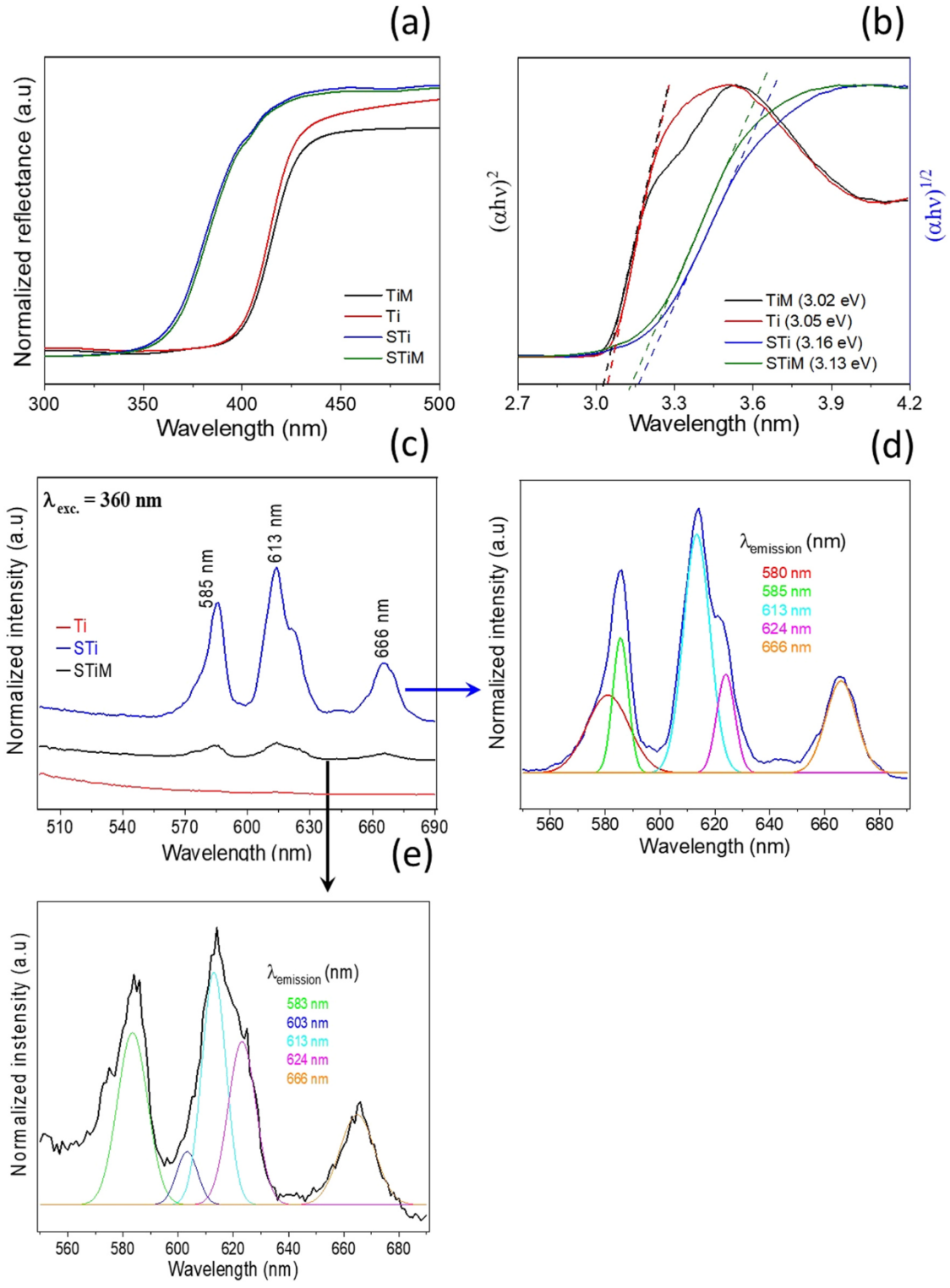

Fig. 5. Diffuse reflectance spectrum (a), bandgap energy (b), PL spectrum with excitation at 360 nm (c). Deconvolution of the PL spectrum obtained with excitation at 360 nm of the STiM (d) and STi (e) samples.

photocatalytic activity of the doped materials under UV-A light radiation. High performance of STiM to remove > 99% of RhB in 30 min was achieved by STi only in the time of 60 min, while the maximum removal by Ti and TiM was 70% in 60 min. These results suggest that the doped materials efficiently promote the separation of charge carriers to oxidize water and, thus, form the reactive oxygen species capable of oxidizing RhB. As holes are responsible for oxidizing H_2O and generating $^{\bullet}OH$, radical probe assays using the coumarin photoluminescence method were performed for all processes and shown in Fig. 6b In the $^{\bullet}OH$ presence, coumarin is converted into Umbelliferone, which has a PL emission spectrum with a peak centered at 454 nm [13,56]. This assay proved that $^{\bullet}OH$ are formed in greater amounts in STiM and lesser amounts in STi, while photolysis and photocatalysis with TiM and Ti were not able to convert coumarin into umbelliferone.

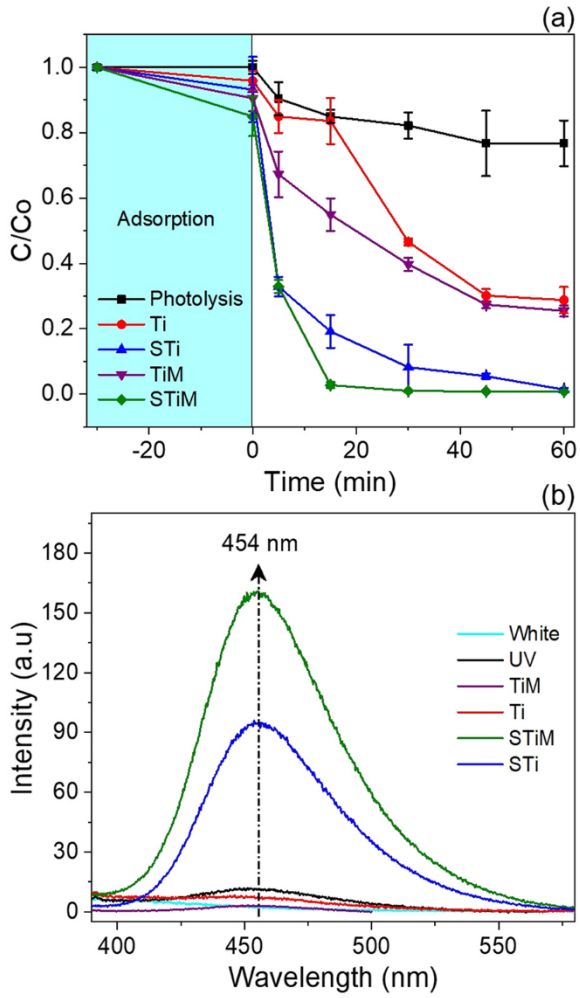

Fig. 6. Photocatalytic degradation curve of RhB (a) PL spectrum of •OH probe assay (b) under UV-A light irradiation.

Compared the efficiency of the photocatalysts obtained in this study with other studies in the literature [57–61], Table 2 shows results of photocatalytic degradation of RhB under different conditions, which were also detailed. The comparative data confirm that even presented a Sm/Ti molar ratio of only 0.05 mol% of for STiM and 0.08 mol% for STi, the materials synthesized in this study showed the high performance to degrade RhB by the photocatalytic process. Even with the comparative data in Table 2, which shows recent studies using RhB as a model molecule to investigate the photoactivity of semiconductors, its use calls for caution [62]. According to Kumar et al. [63], RhB is a photosensitizing compound used to promote electronic excitation in semiconductors through electron donation [63,64]. Thus, photocatalysis is indirect, as RhB is the light-absorbing species instead of the semiconductor. This behavior explains the fact that the Ti sample reaches 70% degradation of RhB in 60 min, although its composition is mostly rutile phase which is not considered photoactive [16,17]. To overcome this limitation associated with RhB, the use of emerging contaminants how ATZ that show insignificant light absorption in the semiconductor excitation wavelength (365 nm for this study) is recommended [62]. Therefore, to investigate in detail the photocatalytic mechanism of different materials and unveil its real photoactivity, the degradation of the emerging contaminant ATZ, which shows greater persistence in the environment than RhB, was investigated in more detail. As the Ti and TiM samples showed the same phase (rutile) composition and were not efficient in the production of hydroxyl radicals, the ATZ photocatalysis assays were conducted in the absence of TiM.

3.2.2. Photocatalytic degradation of ATZ

Fig. 7a showed the C/Co ratio after ATZ photodegradation under UV-A light irradiation (365 nm) at different exposure times. For the time up to 300 min, ATZ removal was only 2% for the photolytic mechanism, confirming that UV-A light energy is not able to efficiently promote the ATZ degradation. This ATZ stability has already been shown in studies conducted by Zhang et al. [14], who found no real removal of ATZ even after 6 h of irradiation under UV-A light (365 nm). For this reason, heterogeneous photocatalysis is one of the main processes applied to achieve the efficient degradation of ATZ under radiation with λ > 365 nm [14,65]. In the present study, the photocatalytic degradation reached an ATZ average removal of 12% in up to 30 min, and it was not possible to define a material with better performance for the respective irradiation time, as shown by the degradation lines accompanied by the respective error bars (Fig. 7a). To the Ti-mediated photocatalytic process, the average degradation showed an improvement of only 3% compared to photolysis and reached a maximum removal of only 5% (average) up to 300 min. This low degradation efficiency in the Ti presence corroborates the characterization data that confirmed the 100% composition of the rutile phase for the respective material. Rutile, even with the lowest bandgap energy (E_{gap} = 2.94 eV) among the materials synthesized in this study, does not present significant photoactivity. This is because photogenerated electrons remain deeply trapped in the structural defects and do not efficiently migrate up to the CB to form reactive oxygen species such as $HO_2^{\bullet-}$, $O_2^{\bullet-}$ which are capable of ATZ degrading [19]. However, a small number of trapped electrons can escape to CB and succinctly promote the photocatalytic degradation of ATZ, which is generally very low for rutile and in this study was only 5% up to 300 min

When analyzing the photocatalytic degradation curves in the STi and STiM presence it is possible to notice a removal efficiency of 30% and 45%, respectively in up to 300 min, which represents an improvement of 25% for STi and 42% for STiM compared to Ti sample. This improvement is a result of the presence of the TiO_2 photoactive polymorphs (anatase and brookite) plus the presence of the Sm that make up the structure of STi and STiM. Unlike rutile, anatase can effectively promote the separation of charge carriers and transfer electrons to CB and thus generate reactive oxygen species to degrade ATZ [19]. As described in the literature, the anatase phase shows its photoactivity in the UV region, where this photocatalyst is widely applied for the degradation of the emerging pollutants [53,66]. Already the brookite can maintain the separation of charge carriers to

Table 2
Results of RhB degradation after photocatalysis by different experimental conditions applying UV irradiation.

Photocatalyst/dosage (mg L^{-1})	RhB (mg L^{-1})/Solution vol. (mL)	Light source	Removal (%)/time (min)	Ref.
MMT-TiO_2/100	5/100	UV-C (254 nm)	97.5/210	[57]
Ag-TiO_2/1000	5/100	UV-C (254 nm)	97/20	[58]
TiO_2-GDY/100	8/1	UV-A (365 nm)	100/60	[59]
I/C-TiO_2/500	20/100	UV-A (400 nm)	100/25	[60]
Co_3O_4@g-C_3N_4/200	20/50	UV ([a])	100/60	[61]
Sm-TiO_2/500	5/10	UV-A (365 nm)	97/15	This study

[a] Unavailable information.

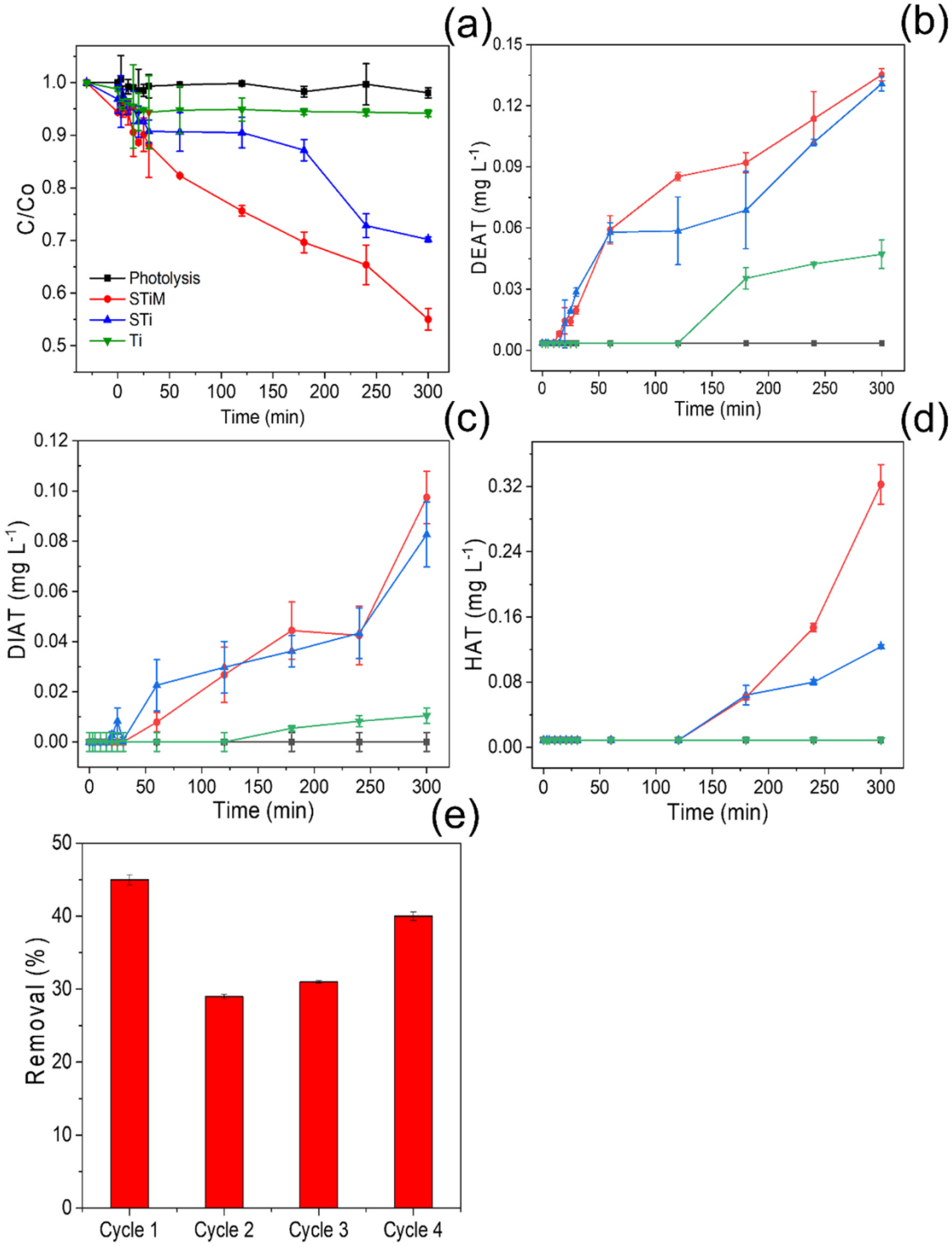

Fig. 7. Degradation curve (C/Co) of ATZ (a), and by-products DEAT (b), DIAT (c) and HAT (d) formation. Reuse study for STiM at 300 min each cycle (f). Conditions: For the radical probe assay: COU = 1.5 mg L^{-1} (10 mL), STiM = 5 mg, Irradiation time = 2 h.

promote the ATZ efficient degradation in both VB and CB. Here, it is important to emphasize that brookite traps photoexcited electrons in its structure defects, however, this trapping occurs at a moderate depth, which allows transfer to the CB due to the multielectron process [18,21]. How shown by the PL data (Fig. 5), the Sm^{3+} dopant effectively contributes to trapping electrons at different energy levels. These electrons trapped in Sm^{3+} showed high recombination for the STi sample compared to STiM, suggesting that in STiM the photoexcited electrons in brookite are transferred to Sm^{3+} and later to anatase, minimizing the recombination processes. Thus, the trapped electrons in Sm^{3+} and brookite increase the concentration of these species in this TiO_2 polymorph and, consequently, the occurrence of the multielectron process efficiently feeds the CB of anatase. As a result, the STiM surface is more efficient in continuously feeding the formation of new redox pairs (h^+/e^-) and thus, promote both ATZ oxidation and reduction reactions. This proposed electron transfer mechanism corroborates the ATZ degradation results, where the C/Co ratio linearly decays up to 300 min for STiM, reaching a maximum

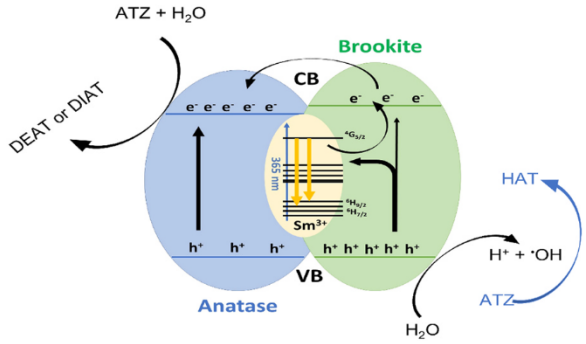

Fig. 8. ATZ photocatalytic degradation mechanism under UV-A light irradiation (365 nm) mediated by the STiM photocatalyst.

removal of 45% to ATZ. Photocatalytic degradation is also observed for STi and reaches a maximum removal of 30% within 300 min. This 15% ATZ degradation efficiency difference between STi and STiM is due to higher recombination and lower amount of brookite present in STi.

In addition to the degraded ATZ, the formation of three of the main by-products (DEAT, DIAT, and HAT) was also monitored to unveil in detail the ATZ degradation mechanism in the presence of different photocatalysts. The literature shows that DEA and DIA are by-products mainly formed by the hydrolysis of ATZ, while HAT is formed by the hydroxylation of halogenated carbon [67,68]. Fig. 7b shows that DEAT starts to be formed between 15 and 20 min of irradiation in the presence of STi and STiM, while in the presence of Ti the by-product starts to be formed after 120 min of irradiation. This behavior is due to the more active surface of STi and STiM, which has a greater amount of trapped electrons in brookite defects. As these materials are doped with Sm^{3+}, the concentration of these electrons increases due to electronic transfer between the energy levels of Sm^{3+} and brookite, allowing the activation of ATZ hydrolysis reactions to form DEA with greater efficiency than found for Ti. As the defects in rutile are deep, excited electrons have greater difficulty in migrating to the Ti surface and activating the ATZ hydrolysis reaction, which occurs after 120 min of irradiation and reaches 35% of the DEAT concentration compared to STi and STiM. Similar behavior is noted for DIAT, which is formed with greater consistency after 60 min of irradiation in the presence of STi and STiM, while in the Ti presence the time is > 120 min (Fig. 7c). Here, the amount of DIAT formed in the Ti presence represents only 13% of the concentration formed in the presence of STi and STiM. As photolysis did not show ATZ degradation, no by-product was detected by HPLC analysis and, therefore, it is possible to conclude that this ATZ degradation mechanism is exclusively photocatalytic and can be represented by Eqs. (1) and (2). For clarity, ATZ = $C_8H_{14}ClN_5$, DEAT = $C_6H_{10}ClN_5$, DIAT = $C_5H_8ClN_5$ and HAT = $C_8H_{15}N_5O$.

$$C_8H_{14}ClN_5(ATZ) + hv\ (365\ nm) + H_2O\ C_6H_{10}ClN_5(DIAT) + C_2H_6O \quad (1)$$

$$C_8H_{14}ClN_5(ATZ) + hv\ (365\ nm) + H_2O\ C_5H_8ClN_5(DEAT) + C_3H_7O \quad (2)$$

Fig. 7d showed that the HAT concentration increases after 120 min of irradiation only in STi and STiM, while no amount of HAT was formed in the Ti presence. Unlike the concentration of DIAT and DEAT which were equivalent for STi and STiM, the HAT concentration was up to 68% higher in the 300 min time for the STiM-mediated photocatalytic process compared to STi. As HAT is a by-product formed after halogenated carbon hydroxylation, it is possible to conclude that this reaction mechanism is dependent on the water oxidation in the holes the VB of the photocatalysts. Thus, this greater amount of HAT formed in STiM is a result of the greater amount of brookite in this material, which feeds the redox reactions by the multielectron process due to trapping in Sm^{3+}/brookite. This behavior allows holes in the VB of STiM to be continuously formed to generate •OH. The characterization results showed that the electron transfer processes are the same for STi and STiM, with the exception that the recombination in STiM is smaller, increasing the lifetime of the holes in this photocatalyst. This assay proved that •OH are formed in greater amounts in STiM and lesser amounts in STi, while photolysis and photocatalysis with Ti were not able to convert coumarin into umbelliferone. Thus, the HAT absence in the Ti-mediated photolytic and photocatalytic processes are justified and the ATZ degradation mechanism to form HAT was represented by the set of Eqs. (3)–(6).

$$STiM/STi + hv(365\ nm) \rightarrow h^+(VB) + e^-(CB) \quad (3)$$

$$h^+(VB) + H_2O \rightarrow {}^{\bullet}OH + H^+ \quad (4)$$

$${}^{\bullet}OH + C_8H_{14}ClN_5(ATZ) \rightarrow C_8H_{15}N_5O(HAT) + Cl^- \quad (5)$$

$$e^-(CB) + C_8H_{14}ClN_5(ATZ) \rightarrow \text{by-products} \quad (6)$$

Fig. 7e showed the ATZ degradation efficiency after 4 application cycles of 300 min. Between the first and second cycles, a 15% drop was verified in the degradation efficiency and it increased again in the following cycles, reaching an ATZ degradation efficiency of 40% after 1200 min. It is noteworthy that no pre-treatment was performed to reapply the materials in subsequent cycles and thus, the variations observed may be related to the presence of adsorbed species. Furthermore, photocatalysis mediated by the multielectron process is dependent on the chemisorption processes of O_2 species or other molecules on the surface of the materials to provide electrons to the electronic levels of the photocatalyst [18]. In the current study, Sm^{3+} was responsible for contributing to this process, but as doping was invariable, future studies will be carried out varying the concentration of the dopant to unravel in greater detail this mechanism aiming at optimizing photocatalytic degradation. Even though it is a mechanism that still requires further studies, especially due to the variation in the Sm^{3+} concentration, Fig. 8 shows a proposal for a photocatalytic mechanism for the ATZ degradation mediated by STi or STiM under UV-A light radiation (365 nm).

Finally, this study showed for the first time that the TiO_2 enhanced photoactivity was obtained by the synergistic use of MW_UV_Vis energies during the synthetic step using an MDEL, and Sm^{3+} doping. Even without optimizing ATZ degradation steps regarding catalyst mass, reaction medium pH, organic pollutant concentration, and other parameters, photocatalytic degradation was

Table 3
Results of ATZ degradation after photocatalysis by different experimental conditions.

Photocatalyst/dosage (mg L^{-1})	ATZ (mg L^{-1})/Solution vol. (mL)	Light source	Removal (%)/time (min)	Ref.
N,F-TiO_2 (NPs)/ 1000	5/10	UV-A (365 nm)	75/120	[69]
TiO_2 (NWs)/1000	5/10	UV-A (365 nm)	56/60	[70]
Pbi-ZnO-g-C3N4/1000	10/100	solar simulator	85/260	[71]
ZnIn2S4/500	2 /[a]	UV_Vis (380–820 nm)	87/300	[72]
Nano-TiO2/100	5/300	UV-A (365 nm)	31/60	[73]
STiM/500	10/10	UV-A (365 nm)	45/300	This study

[a] Unavailable information.

achieved and compared to other studies of the literature [69–73] (Table 3). Thus, future studies can explore other synthetic parameters to increase defects in the material's structure, as well as seek the optimized condition for the photocatalytic degradation step aiming at the remediation of water contaminated with ATZ. In addition, the quantitative monitoring of the by-products allowed to propose a mechanism of photocatalytic activity of the materials consistent with all material characterization results and analysis of the compounds present in the reaction medium.

4. Conclusion

In this study, two energy sources, namely a microwave and an MDEL, were applied for the first time to synthesize Sm-doped TiO_2 in hydrothermal conditions. The Sm^{3+} inhibited the conversion of anatase to rutile and a mixture of the polymorphs brookite and anatase was confirmed in the proportion of 8% for STi and 12% for STiM. The highest percentage of brookite in STiM was a result of the more reductive condition imposed by MDEL, as the emission spectra with $\lambda = 193–247$ nm can promote redox reactions to increase the concentration of electrons in the reaction medium. Rietveld refinement analyzes were not able to detect large perturbations in the TiO_2 network, indicating that Sm^{3+} replaced Ti^{4+} through substitutional doping. The presence of Sm in the STi and STiM samples was evident by the PL spectrum emission under light excitation at 360 nm, which shows the band emissions at 585, 613, and 666 nm characteristics of Sm electronic transitions. Furthermore, we proved the Sm/Ti doping showed 0.08 mol% for STi and 0.05 mol% for STiM by ICP OES analysis. In the application step, only the photocatalytic process was able to degrade ATZ under UV-A(365 nm) light irradiation, achieving removal of 5% for Ti, 30% for STi, and 45% for STiM in 300 min. The best performance for doped materials is due to the ability of Sm^{3+} and brookite to trap photoexcited electrons in structural defects to increase the lifetime of redox pairs. As the recombination rates in STi are higher, STiM proved to be more efficient to increase the lifetime of redox pairs due to the higher amount of brookite. The by-products DEAT and DIAT were obtained by the ability of anatase to activate the hydrolysis reaction of ATZ, while the HAT formation was the result of the ATZ oxidation by the $^{\bullet}OH$ formed in the VB of brookite. Probe assays for radicals proved that STiM is more efficient to form these reactive species, explaining the fact that STiM forms an amount of HAT 68% higher than that verified for STi. Finally, the reuse studies showed that the materials remain photoactive even after 4 application cycles (1200 min), indicating that the synthetic strategy adopted in this study can be an excellent alternative to obtain new materials with optimized photocatalytic properties.

CRediT authorship contribution statement

All authors contributed to the study conception and design. **Ailton José Moreira:** Methodology, Investigation, Formal analysis, Writing – original draft. **Dyovani Coelho:** Investigation, Writing – review & editing. **Jeferson A. Dias:** Investigation, Writing – review & editing. **Lucia H. Mascaro:** Writing – review & editing. **Gian P.G. Freschi:** Writing – review & editing. **Valmor R. Mastelaro:** Investigation, Writing – review & editing. **Ernesto C. Pereira:** Writing, Conceptualization, Supervision. All authors commented on previous versions of the manuscript. All authors read and approved the final manuscript.

Declaration of Competing Interest

The authors declare that they have no known competing financial interests or personal relationships that could have appeared to influence the work reported in this paper.

Acknowledgments

This work was financially supported by Coordenação de Aperfeiçoamento de Pessoal de Nível Superior (CAPES, grant # 88887.368533/2019-00 and Code # 001), Fundação de Amparo à Pesquisa do Estado de São Paulo (grants: 2013/07296-2, 2014/50249-8, 2017/11986-5), Conselho Nacional de Desenvolvimento Científico e Tecnológico (CNPq), and Shell.

Appendix A. Supporting information

Supplementary data associated with this article can be found in the online version at doi:10.1016/j.jallcom.2022.164217.

References

[1] U. Mc Carthy, I. Uysal, R. Badia-Melis, S. Mercier, C. O'Donnell, A. Ktenioudaki, Global food security – issues, challenges and technological solutions, Trends Food Sci. Technol. 77 (2018) 11–20, https://doi.org/10.1016/j.tifs.2018.05.002
[2] T.A. da, C. Dias, E.E.S. Lora, D.M.Y. Maya, O.A. del Olmo, Global potential assessment of available land for bioenergy projects in 2050 within food security limits, Land Use Policy 105 (2021) 105346, https://doi.org/10.1016/j.landusepol.2021.105346
[3] M. Syafrudin, R.A. Kristanti, A. Yuniarto, T. Hadibarata, J. Rhee, W.A. Al-onazi, T.S. Algarni, A.H. Almarri, A.M. Al-Mohaimeed, Pesticides in Drinking Water—a review, Int. J. Environ. Res. Public Health 18 (2021) 468, https://doi.org/10.3390/ijerph18020468
[4] C.M. Raffa, F. Chiampo, Bioremediation of agricultural soils polluted with pesticides: a review, Bioengineering 8 (2021) 92, https://doi.org/10.3390/bioengineering8070092
[5] F.P. de Albuquerque, J.L. de Oliveira, V. Moschini-Carlos, L.F. Fraceto, An overview of the potential impacts of atrazine in aquatic environments: perspectives for tailored solutions based on nanotechnology, Sci. Total Environ. 700 (2020) 134868, https://doi.org/10.1016/j.scitotenv.2019.134868
[6] R. Frassanito, G. De Socio, D. Laura, D. Rotilio, Dtermination of s -Triazine Metabolites: A Mass Spectrometric Investigation, Je. Agric. Food Chem. 44 (1996) 2282–2286, https://doi.org/10.1021/jf950293t
[7] Š. Klementová, L. Hornychová, M. Šorf, J. Zemanová, D. Kahoun, Toxicity of atrazine and the products of its homogeneous photocatalytic degradation on the aquatic organisms Lemna minor and Daphnia magna, Environ. Sci. Pollut. Res. 26 (2019) 27259–27267, https://doi.org/10.1007/s11356-019-05710-0
[8] L. Yang, Y. Zhang, Effects of atrazine and its two major derivatives on the photosynthetic physiology and carbon sequestration potential of a marine diatom, Ecotoxicol. Environ. Saf. 205 (2020) 111359, https://doi.org/10.1016/j.ecoenv.2020.111359
[9] S. Klementova, M. Zlamal, Photochemical degradation of triazine herbicides - comparison of homogeneous and heterogeneous photocatalysis, Photochem. Photobiol. Sci. 12 (2013) 660–663, https://doi.org/10.1039/c2pp25223f
[10] E.C. Paris, J.O.D. Malafatti, C.R. Sciena, L.F.N. Junior, A. Zenatti, M.T. Escote, A.J. Moreira, G.P.G. Freschi, Nb2O5 nanoparticles decorated with magnetic ferrites for wastewater photocatalytic remediation, Environ. Sci. Pollut. Res. (2020), https://doi.org/10.1007/s11356-020-11262-5
[11] C.G. Renda, C.P. Contreras Medrano, L.J.D. Costa, F.J. Litterst, E.M.B. Saitovitch, C.J. Magon, A.J. Gualdi, T. Venâncio, R. Bertholdo, A.J. Moreira, G.P.G. Freschi, A. de Almeida Lucas, Role of ferrocene-derived iron species in the catalytic graphitization of novolak resins, J. Mater. Sci. 56 (2021) 1298–1311, https://doi.org/10.1007/s10853-020-05312-z
[12] H. Ren, Y. Su, X. Han, R. Zhou, Synthesis and characterization of saponin-modified Fe3O4 nanoparticles as heterogeneous Fenton-catalyst with enhanced degradation of p-nitrophenol, J. Chem. Technol. Biotechnol. 92 (2017) 1421–1427, https://doi.org/10.1002/jctb.5139
[13] E.T. de Jesus, A.J. Moreira, M.C. Sá, G.P.G. Freschi, M.R. Joya, M.S. Li, E.C. Paris, Potential of Nb2O5 nanofibers in photocatalytic degradation of organic pollutants, Environ. Sci. Pollut. Res. (2021), https://doi.org/10.1007/s11356-021-15435-8
[14] Y. Zhang, C. Han, M.N. Nadagouda, D.D. Dionysiou, The fabrication of innovative single crystal N,F-codoped titanium dioxide nanowires with enhanced photocatalytic activity for degradation of atrazine, Appl. Catal. B Environ. 168–169 (2015) 550–558, https://doi.org/10.1016/j.apcatb.2015.01.009

[15] C. Carlucci, B.F. Scremin, T. Sibillano, C. Giannini, E. Filippo, P. Perulli, A.L. Capodilupo, G.A. Corrente, G. Ciccarella, Microwave-assisted synthesis of boron-modified TiO 2 nanocrystals, Inorganics 2 (2014) 264–277, https://doi.org/10.3390/inorganics2020264

[16] D. Dambournet, I. Belharouak, K. Amine, Tailored preparation methods of TiO2 anatase, rutile, brookite: mechanism of formation and electrochemical properties, Chem. Mater. 22 (2010) 1173–1179, https://doi.org/10.1021/cm902613h

[17] R. Kaplan, B. Erjavec, G. Dražić, J. Grdadolnik, A. Pintar, Simple synthesis of anatase/rutile/brookite TiO < inf > 2 < /inf > nanocomposite with superior mineralization potential for photocatalytic degradation of water pollutants, Appl. Catal. B Environ. 181 (2016) 465–474, https://doi.org/10.1016/j.apcatb.2015.08.027

[18] J.J.M. Vequizo, H. Matsunaga, T. Ishiku, S. Kamimura, T. Ohno, A. Yamakata, Trapping-induced enhancement of photocatalytic activity on brookite TiO 2 powders: comparison with anatase and rutile TiO2 powders, ACS Catal. 7 (2017) 2644–2651, https://doi.org/10.1021/acscatal.7b00131

[19] A. Yamakata, J.J.M. Vequizo, Curious behaviors of photogenerated electrons and holes at the defects on anatase, rutile, and brookite TiO2 powders: a review, J. Photochem. Photobiol. C Photochem. Rev. 40 (2019) 234–243, https://doi.org/10.1016/j.jphotochemrev.2018.12.001

[20] N.S. Allen, N. Mahdjoub, V. Vishnyakov, P.J. Kelly, R.J. Kriek, The effect of crystalline phase (anatase, brookite and rutile) and size on the photocatalytic activity of calcined polymorphic titanium dioxide (TiO2), Polym. Degrad. Stab. 150 (2018) 31–36, https://doi.org/10.1016/j.polymdegradstab.2018.02.008

[21] M. Monai, T. Montini, P. Fornasiero, Brookite: nothing New under the Sun? Catalysts 7 (2017) 304, https://doi.org/10.3390/catal7100304

[22] S.G. Kumar, K.S.R.K. Rao, Polymorphic phase transition among the titania crystal structures using a solution-based approach: from precursor chemistry to nucleation process, Nanoscale 6 (2014) 11574–11632, https://doi.org/10.1039/C4NR01657B

[23] K. Lee, A. Mazare, P. Schmuki, One-dimensional titanium dioxide nanomaterials: nanotubes, Chem. Rev. 114 (2014) 9385–9454, https://doi.org/10.1021/cr500061m

[24] E.M. Samsudin, S.B. Abd Hamid, J.C. Juan, W.J. Basirun, G. Centi, Synergetic effects in novel hydrogenated F-doped TiO 2 photocatalysts, Appl. Surf. Sci. 370 (2016) 380–393, https://doi.org/10.1016/j.apsusc.2016.02.172

[25] H. Hori, M. Takashima, M. Takase, B. Ohtani, Kinetic analysis supporting multi-electron reduction of oxygen in bismuth tungstate-photocatalyzed oxidation of organic compounds, Catal. Today 313 (2018) 218–223, https://doi.org/10.1016/j.cattod.2018.01.001

[26] F. Peng, H. Gao, G. Zhang, Z. Zhu, J. Zhang, Q. Liu, Synergistic effects of Sm and C Co-doped mixed phase crystalline TiO2 for visible light photocatalytic activity, Materials 10 (2017) 209, https://doi.org/10.3390/ma10020209

[27] Li-Yuan Zhang, X.-J. Wan, Y.-H. You, S.-Q. Ruan, T. Luo, Q. Yang, Synthesis of fibrous Sm3+-doped titanium dioxide using collagen fiber As a template and its photocatalytic properties, Russ. J. Phys. Chem. A 93 (2019) 2087–2096, https://doi.org/10.1134/S0036024419100340

[28] T.A. Kandiel, L. Robben, A. Alkaim, D. Bahnemann, Brookite versus anatase TiO 2 photocatalysts: phase transformations and photocatalytic activities, Photochem. Photobiol. Sci. 12 (2013) 602–609, https://doi.org/10.1039/C2PP25217A

[29] S.M. El-Sheikh, T.M. Khedr, G. Zhang, V. Vogiazi, A.A. Ismail, K. O'Shea, D.D. Dionysiou, Tailored synthesis of anatase–brookite heterojunction photocatalysts for degradation of cylindrospermopsin under UV–Vis light, Chem. Eng. J. 310 (2017) 428–436, https://doi.org/10.1016/j.cej.2016.05.007

[30] A. Moreira, A. Borges, B. de Sousa, V. de Mendonça, C. Freschi, G. Freschi, Photodegradation of fluoxetine applying different photolytic reactors: evaluation of the process efficiency and mechanism, J. Braz. Chem. Soc. 30 (2018) 1010–1024, https://doi.org/10.21577/0103-5053.20180250

[31] A.J. Moreira, A.C. Borges, B.B. de Souza, L.R. Barbosa, V.R. de Mendonça, C.D. Freschi, G.P.G. Freschi, Microwave discharge electrodeless mercury lamp (Hg-MDEL): an energetic, mechanistic and kinetic approach to the degradation of Prozac®, J. Environ. Chem. Eng. 7 (2019) 102916, https://doi.org/10.1016/j.jece.2019.102916

[32] S. Horikoshi, A. Tsuchida, T. Shinomiya, N. Serpone, Microwave discharge electrodeless lamps (MDELs). Part IX. A novel MDEL photoreactor for the photolytic and chemical oxidation treatment of contaminated wastewaters, Photochem. Photobiol. Sci. 14 (2015) 2187–2194, https://doi.org/10.1039/c5pp00297d

[33] L. Vivas, G.E. Delgado, P. Leret, J.F. Fernández, J.L. Costa-Krämer, P. Silva, Electron paramagnetic resonance study of hopping in CCTO mixed with TiO2, J. Alloy. Compd. 692 (2017) 212–218, https://doi.org/10.1016/j.jallcom.2016.09.034

[34] T. Mashimo, R. Bagum, Y. Ogata, M. Tokuda, M. Okube, K. Sugiyama, Y. Kinemuchi, H. Isobe, A. Yoshiasa, Structure of single-crystal rutile (TiO 2) prepared by high-temperature ultracentrifugation, Cryst. Growth Des. 17 (2017) 1460–1464, https://doi.org/10.1021/acs.cgd.6b01818

[35] D. Dambournet, K.W. Chapman, M.V. Koudriachova, P.J. Chupas, I. Belharouak, K. Amine, Combining the pair distribution function and computational methods to understand lithium insertion in brookite (TiO 2), Inorg. Chem. 50 (2011) 5855–5857, https://doi.org/10.1021/ic2004326

[36] B.H. Toby, EXPGUI, a graphical user interface for GSAS, J. Appl. Crystallogr. 34 (2001) 210–213, https://doi.org/10.1107/S0021889801002242

[37] C.F. Macrae, I. Sovago, S.J. Cottrell, P.T.A. Galek, P. McCabe, E. Pidcock, M. Platings, G.P. Shields, J.S. Stevens, M. Towler, P.A. Wood, Mercury 4.0: from visualization to analysis, design and prediction, J. Appl. Crystallogr. 53 (2020) 226–235, https://doi.org/10.1107/S1600576719014092

[38] A.L. Patterson, The scherrer formula for X-ray particle size determination, Phys. Rev. 56 (1939) 978–982, https://doi.org/10.1103/PhysRev.56.978

[39] R. López, R. Gómez, Band-gap energy estimation from diffuse reflectance measurements on sol-gel and commercial TiO 2: A comparative study, J. Sol-Gel Sci. Technol. 61 (2012) 1–7, https://doi.org/10.1007/s10971-011-2582-9

[40] A.J. Moreira, J.O.D. Malafatti, T.R. Giraldi, E.C. Paris, E.C. Pereira, V.R. de Mendonça, V.R. Mastelaro, G.P.G. Freschi, Prozac® photodegradation mediated by Mn-doped TiO < inf > 2 < /inf > nanoparticles: evaluation of by-products and mechanisms proposal, J. Environ. Chem. Eng. 8 (2020), https://doi.org/10.1016/j.jece.2020.104543

[41] J.A. Dias, A.L.F. Freire, I. Girotto, C. Del Roveri, V.R. Mastelaro, E.C. Paris, T.R. Giraldi, Phase evolution and optical properties of nanometric Mn-doped TiO2 pigments, Mater. Today Commun. 27 (2021) 102295, https://doi.org/10.1016/j.mtcomm.2021.102295

[42] G.M. Neelgund, S.A. Shivashankar, B.K. Chethana, P.P. Sahoo, K.J. Rao, Nanocrystalline TiO2 preparation by microwave route and nature of anatase-rutile phase transition in nano TiO2, Bull. Mater. Sci. 34 (2011) 1163–1171, https://doi.org/10.1007/s12034-011-0165-6

[43] R.D. Shannon, Revised effective ionic radii and systematic studies of interatomic distances in halides and chalcogenides, Acta Crystallogr. Sect. A 32 (1976) 751–767, https://doi.org/10.1107/S0567739476001551

[44] N. Serpone, S. Horikoshi, A.V. Emeline, Microwaves in advanced oxidation processes for environmental applications. A brief review, J. Photochem. Photobiol. C Photochem. Rev. 11 (2010) 114–131, https://doi.org/10.1016/j.jphotochemrev.2010.07.003

[45] D.R. Hummer, J.D. Kubicki, P.R.C. Kent, J.E. Post, P.J. Heaney, Origin of nanoscale phase stability reversals in titanium oxide polymorphs, J. Phys. Chem. C 113 (2009) 4240–4245, https://doi.org/10.1021/jp811332w

[46] J.H. Leal, Y. Cantu, D.F. Gonzalez, J.G. Parsons, Brookite and anatase nanomaterial polymorphs of TiO2 synthesized from TiCl3, Inorg. Chem. Commun. 84 (2017) 28–32, https://doi.org/10.1016/j.inoche.2017.07.014

[47] L. Li, C. Liu, Facile synthesis of anatase–Brookite mixed-phase N-doped TiO 2 nanoparticles with high visible-light photocatalytic activity, Eur. J. Inorg. Chem. 2009 (2009) 3727–3733, https://doi.org/10.1002/ejic.200900369

[48] Q.R. Deng, X.H. Xia, M.L. Guo, Y. Gao, G. Shao, Mn-doped TiO2 nanopowders with remarkable visible light photocatalytic activity, Mater. Lett. 65 (2011) 2051–2054, https://doi.org/10.1016/j.matlet.2011.04.010

[49] Z.P. Tshabalala, K. Shingange, F.R. Cummings, O.M. Ntwaeaborwa, G.H. Mhlongo, D.E. Motaung, Ultra-sensitive and selective NH3 room temperature gas sensing induced by manganese-doped titanium dioxide nanoparticles, J. Colloid Interface Sci. 504 (2017) 371–386, https://doi.org/10.1016/j.jcis.2017.05.061

[50] Y. Uwamino, T. Ishizuka, H. Yamatera, X-ray photoelectron spectroscopy of rare-earth compounds, J. Electron Spectrosc. Relat. Phenom. 34 (1984) 67–78, https://doi.org/10.1016/0368-2048(84)80060-2

[51] H. Peng, R. Guo, H. Lin, Photocatalytic reduction of CO_2 over Sm-doped TiO2 nanoparticles, J. Rare Earths 38 (2020) 1297–1304, https://doi.org/10.1016/j.jre.2019.12.010

[52] J. Ma, J. Chu, L. Qiang, J. Xue, Effect of different calcination temperatures on the structural and photocatalytic performance of Bi-TiO2/SBA-15, Int. J. Photoenergy 2013 (2013) 1–10, https://doi.org/10.1155/2013/875456

[53] A.J. Moreira, L.O. Campos, C.P. Maldi, J.A. Dias, E.C. Paris, T.R. Giraldi, G.P.G. Freschi, Photocatalytic degradation of Prozac® mediated by TiO2 nanoparticles obtained via three synthesis methods: sonochemical, microwave hydrothermal, and polymeric precursor, Environ. Sci. Pollut. Res. 27 (2020) 27032–27047, https://doi.org/10.1007/s11356-020-08798-x

[54] H. Zhang, Y. Sheng, Y. Song, H. Li, J. Huang, K. Zheng, Q. Huo, X. Xu, H. Zou, Uniform hollow TiO2:Sm3+ spheres: solvothermal synthesis and luminescence properties, Powder Technol. 239 (2013) 403–408, https://doi.org/10.1016/j.powtec.2013.02.010

[55] B.M.M. Faustino, P.J.S. Foot, R.A. Kresinski, Synthesis and photoluminescent properties of Sm3+-doped SnO2 nanoparticles, Ceram. Int. 42 (2016) 18474–18478, https://doi.org/10.1016/j.ceramint.2016.08.183

[56] J.O.D. Malafatti, A.J. Moreira, C.R. Sciena, T.E.M. Silva, G.P.G. Freschi, E.C. Pereira, E.C. Paris, Prozac® removal promoted by HAP:Nb2O5 nanoparticles system: by-products, mechanism, and cytotoxicity assessment, J. Environ. Chem. Eng. (2020) 104820, https://doi.org/10.1016/j.jece.2020.104820

[57] T.B.T. Dao, T.T.L. Ha, T. Do Nguyen, H.N. Le, C.N. Ha-Thuc, T.M.L. Nguyen, P. Perre, D.M. Nguyen, Effectiveness of photocatalysis of MMT-supported TiO2 and TiO2 nanotubes for rhodamine B degradation, Chemosphere 280 (2021) 130802, https://doi.org/10.1016/j.chemosphere.2021.130802

[58] I. Ellouzi, A. Bouddouch, B. Bakiz, A. Benlhachemi, H. Abou Oualid, Glucose-assisted ball milling preparation of silver-doped biphasic TiO2 for efficient photodegradation of Rhodamine B: effect of silver-dopant loading, Chem. Phys. Lett. 770 (2021) 138456, https://doi.org/10.1016/j.cplett.2021.138456

[59] R. Wang, M. Shi, F. Xu, Y. Qiu, P. Zhang, K. Shen, Q. Zhao, J. Yu, Y. Zhang, Graphdiyne-modified TiO2 nanofibers with osteoinductive and enhanced photocatalytic antibacterial activities to prevent implant infection, Nat. Commun. 11 (2020) 4465, https://doi.org/10.1038/s41467-020-18267-1

[60] J.-C. Wang, H.-H. Lou, Z.-H. Xu, C.-X. Cui, Z.-J. Li, K. Jiang, Y.-P. Zhang, L.-B. Qu, W. Shi, Natural sunlight driven highly efficient photocatalysis for simultaneous degradation of rhodamine B and methyl orange using I/C codoped TiO2 photocatalyst, J. Hazard. Mater. 360 (2018) 356–363, https://doi.org/10.1016/j.jhazmat.2018.08.008

[61] I. Rabani, R. Zafar, K. Subalakshmi, H.-S. Kim, C. Bathula, Y.-S. Seo, A facile mechanochemical preparation of Co3O4@g-C3N4 for application in supercapacitors and degradation of pollutants in water, J. Hazard. Mater. 407 (2021) 124360, https://doi.org/10.1016/j.jhazmat.2020.124360

[62] N. Barbero, D. Vione, Why dyes should not be used to test the photocatalytic activity of semiconductor oxides, Environ. Sci. Technol. 50 (2016) 2130–2131, https://doi.org/10.1021/acs.est.6b00213
[63] V. Kumar, R. Gupta, A. Bansal, Influence of RhB dye concentration on ZnS nanoflowers decorated TiO2 photoanode in dye sensitized solar cell, Mater. Today Proc. 44 (2021) 1163–1168, https://doi.org/10.1016/j.matpr.2020.11.234
[64] M. Akhtaruzzaman, M. Shahiduzzaman, V. Selvanathan, K. Sopian, M.I. Hossain, N. Amin, A.K.M. Hasan, Enhancing spectral response towards high-performance dye-sensitised solar cells by multiple dye approach: a comprehensive review, Appl. Mater. Today 25 (2021) 101204, https://doi.org/10.1016/j.apmt.2021.101204
[65] C.C. Chen, J. Shaya, H.J. Fan, Y.K. Chang, H.T. Chi, C.S. Lu, Silver vanadium oxide materials: Controlled synthesis by hydrothermal method and efficient photocatalytic degradation of atrazine and CV dye, Sep. Purif. Technol. 206 (2018) 226–238, https://doi.org/10.1016/j.seppur.2018.06.011
[66] A.J. Moreira, S.R.R. Padilha, V.R. de Mendonça, E.C. Paris, C. Ribeiro, G.P.G. Freschi, T.R. Giraldi, Photoactivity of TiO2 nanoparticles covered with nitro group in fluoxetine and rhodamine-B degradation, Desalin. Water Treat. 205 (2020) 252–263, https://doi.org/10.5004/dwt.2020.26379
[67] A.J. Moreira, B.S. Pinheiro, A.F. Araújo, G.P.G. Freschi, Evaluation of atrazine degradation applied to different energy systems, Environ. Sci. Pollut. Res. 23 (2016) 18502–18511, https://doi.org/10.1007/s11356-016-6831-x
[68] A.J. Moreira, A.C. Borges, L.F.C. Gouvea, T.C.O. MacLeod, G.P.G. Freschi, The process of atrazine degradation, its mechanism, and the formation of metabolites using UV and UV/MW photolysis, J. Photochem. Photobiol. A Chem. 347 (2017) 160–167, https://doi.org/10.1016/j.jphotochem.2017.07.022
[69] Y. Zhang, C. Han, M.N. Nadagouda, D.D. Dionysiou, The fabrication of innovative single crystal N,F-codoped titanium dioxide nanowires with enhanced photocatalytic activity for degradation of atrazine, Appl. Catal. B Environ. 168–169 (2015) 550–558, https://doi.org/10.1016/j.apcatb.2015.01.009
[70] Y. Zhang, C. Han, G. Zhang, D.D. Dionysiou, M.N. Nadagouda, PEG-assisted synthesis of crystal TiO2 nanowires with high specific surface area for enhanced photocatalytic degradation of atrazine, Chem. Eng. J. 268 (2015) 170–179, https://doi.org/10.1016/j.cej.2015.01.006
[71] X. An, H. Wang, C. Dong, P. Jiang, Z. Wu, B. Yu, Core-shell P-laden biochar/ZnO/g-C3N4 composite for enhanced photocatalytic degradation of atrazine and improved P slow-release performance, J. Colloid Interface Sci. 608 (2022) 2539–2548, https://doi.org/10.1016/j.jcis.2021.10.166
[72] L. Bo, H.D. Kiriarachchi, J.A. Bobb, A.A. Ibrahim, M.S. El-shall, Preparation, activity, and mechanism of ZnIn2S4-based catalysts for photocatalytic degradation of atrazine in aqueous solution, J. Water Process Eng. 36 (2020) 101334, https://doi.org/10.1016/j.jwpe.2020.101334
[73] N. Hu, Y. Xu, C. Sun, L. Zhu, S. Sun, Y. Zhao, C. Hu, Removal of atrazine in catalytic degradation solutions by microalgae Chlorella sp. and evaluation of toxicity of degradation products via algal growth and photosynthetic activity, Ecotoxicol. Environ. Saf. 207 (2021) 111546, https://doi.org/10.1016/j.ecoenv.2020.111546